

# Scalable Synthesis of Ultrathin $\text{Mn}_3\text{N}_2$ Exhibiting Room-Temperature Antiferromagnetism

Xu Xiao, Patrick Urbankowski, Kanit Hantanasirisakul, Yao Yang, Stephen Sasaki, Long Yang, Chi Chen, Hao Wang, Ling Miao, Sarah H. Tolbert, Simon J. L. Billinge, Héctor D. Abruña, Steven J. May, and Yury Gogotsi\*

Ultrathin and 2D magnetic materials have attracted a great deal of attention recently due to their potential applications in spintronics. Only a handful of stable ultrathin magnetic materials have been reported, but their high-yield synthesis remains a challenge. Transition metal (e.g., manganese) nitrides are attractive candidates for spintronics due to their predicted high magnetic transition temperatures. Here, a lattice matching synthesis of ultrathin  $\text{Mn}_3\text{N}_2$  is employed. Taking advantage of the lattice match between a KCl salt template and  $\text{Mn}_3\text{N}_2$ , this method yields the first ultrathin magnetic metal nitride via a solution-based route.  $\text{Mn}_3\text{N}_2$  flakes show intrinsic magnetic behavior even at 300 K, enabling potential room-temperature applications. This synthesis procedure offers an approach to the discovery of other ultrathin or 2D metal nitrides.

## 1. Introduction

In the past decade, 2D or atomically thin planar materials have attracted great attention due to their unusual physical and chemical properties.<sup>[1,2]</sup> Many new devices for electronics, energy harvesting and storage, plasmonics, etc., have been developed by virtue of the exploration of atomically thin materials, such as graphene,<sup>[3]</sup> transition metal dichalcogenides,<sup>[4]</sup> and black phosphorus.<sup>[5]</sup> However, the development of ultrathin 2D magnetic materials, potentially important building blocks for spintronics, is still at its initial stage and only a handful of materials have

been reported.<sup>[6–11]</sup> A smaller number of them are intrinsically magnetic. Even with these candidates, many scientific and technological challenges remain unresolved. For example, most synthesized 2D magnets show a low magnetic transition temperature (typically, below 100 K) and cannot be operated at room temperature.<sup>[6–8]</sup> Very recently, the first room-temperature ferromagnetic 2D material,  $\text{VSe}_2$ , was reported,<sup>[12]</sup> but to date, no ultrathin 2D flakes that maintain their antiferromagnetic coupling in finite size at room temperature have been reported. In addition, 2D magnetic materials reported so far are sensitive to degradation at atmospheric conditions and require operation

in an inert atmosphere. As a result, environmental and operating issues limit their practical applications. Consequently, it is important to find a high-yield method to obtain stable atomically thin magnetic materials that are operable at and above room temperature.

Transition metal nitrides (TMNs) are promising candidates, because various nitride MXenes have been predicted to have magnetic properties.<sup>[13,14]</sup> Among TMNs, manganese nitride ( $\text{Mn}_3\text{N}_2$ ) is a high-temperature antiferromagnetic material with a Néel temperature around 925 K.<sup>[15]</sup> Importantly, its intrinsic magnetism could be used for both fundamental studies of

Dr. X. Xiao, P. Urbankowski, K. Hantanasirisakul, Dr. C. Chen,  
Dr. H. Wang, Prof. S. J. May, Prof. Y. Gogotsi  
Department of Materials Science and Engineering  
and A. J. Drexel Nanomaterials Institute  
Drexel University  
Philadelphia, PA 19104, USA  
E-mail: gogotsi@drexel.edu  
Y. Yang, Prof. H. D. Abruña  
Department of Chemistry and Chemical Biology  
Cornell University  
Ithaca, NY 14853, USA  
S. Sasaki, Prof. S. H. Tolbert  
Department of Chemistry and Biochemistry and California  
NanoSystems Institute  
University of California, Los Angeles  
Los Angeles, CA 90095, USA

L. Yang, Prof. S. J. L. Billinge  
Department of Applied Physics and Applied Mathematics  
Columbia University  
New York, NY 10027, USA  
Dr. C. Chen, Prof. L. Miao  
School of Optical and Electronic Information  
Huazhong University of Science and Technology  
Wuhan, Hubei 430074, China  
Prof. S. J. L. Billinge  
Condensed Matter Physics and Materials Science Department  
Brookhaven National Laboratory  
Upton, NY 11973, USA

 The ORCID identification number(s) for the author(s) of this article can be found under <https://doi.org/10.1002/adfm.201809001>.

DOI: 10.1002/adfm.201809001

the physics in ultrathin and bulk magnetic materials, and for practical applications. However, achieving a 2D morphology via nonvapor phase approaches is challenging, since the bulk form of  $\text{Mn}_3\text{N}_2$  is not layered and therefore cannot be exfoliated. This is a common issue in ultrathin 2D or 2D-like TMNs, and because of this, only a few of these materials have been reported, such as  $\text{Ti}_4\text{N}_3$ ,<sup>[16]</sup>  $\text{Mo}_2\text{N}$ , and  $\text{V}_2\text{N}$  MXene,<sup>[17]</sup>  $\text{MoN}$ ,<sup>[18]</sup> and  $\text{W}_2\text{N}$ .<sup>[18]</sup> Recently, a high-yield salt-templating method for the synthesis of atomically thin TMNs by ammoniating their metal oxide counterparts was demonstrated.<sup>[18,19]</sup> This provides a viable route to obtain ultrathin flakes of a TMN with room-temperature magnetism.

In this work, we use the salt-templating method to synthesize ultrathin  $\text{Mn}_3\text{N}_2$  flakes (labeled as 2D  $\text{Mn}_3\text{N}_2$ ). Since metal oxides are fairly stable and the formation of TMNs by ammoniation or nitridation always needs high temperatures, instead of the reduction of oxide, we chose manganese chloride as the precursor, which can be directly ammoniated to form 2D metal nitride. This one-step synthesis may expand the family of 2D metal nitrides if the right precursors and templates are identified. The schematic of synthesis of 2D  $\text{Mn}_3\text{N}_2$  is shown in Figure 1. First, a  $\text{MnCl}_2$  solution in ethanol was coated onto the

surface of the KCl salt template (Figure S1, Supporting Information) and dried to form a thin layer of  $\text{MnCl}_2$  on KCl (labeled as  $\text{MnCl}_2@\text{KCl}$ ). Using a  $\text{MnCl}_2$  solution in ethanol prevented the formation of large particles.<sup>[20]</sup> The ratio of solution to salt controlled the thickness of the layer (see details in Figure S2 in the Supporting Information and the Supporting Note). In the actual synthesis, the transparent  $\text{MnCl}_2$  precursor solution was poured into 200 g KCl (Figure 1b), and the  $\text{MnCl}_2@\text{KCl}$  powder was dried and treated at 750 °C under a constant flow of ammonia. During the ammoniation reaction, the  $\text{MnCl}_2@\text{KCl}$  transformed into  $\text{Mn}_3\text{N}_2@\text{KCl}$  (light grayish powder, Figure 1c). After transformation, the KCl salt template was washed with deionized (DI) water to obtain 2D  $\text{Mn}_3\text{N}_2$  (Figure 1e; Figure S3, Supporting Information). 2D  $\text{Mn}_3\text{N}_2$  dispersed well in DI water to form a dark colloidal solution as confirmed by the Tyndall effect (Figure 1f). The KCl was recycled by collecting and recrystallizing its solution (Figure S4, Supporting Information). The proposed growth mechanism is salt-templated growth.<sup>[20]</sup> It is worth mentioning that the crystal structures of  $\text{Mn}_3\text{N}_2$  and KCl have several features in common. In the (001) plane, both of them show square symmetry with similar lattice parameters (lattice mismatch around 3.3%, Figure S5, Supporting

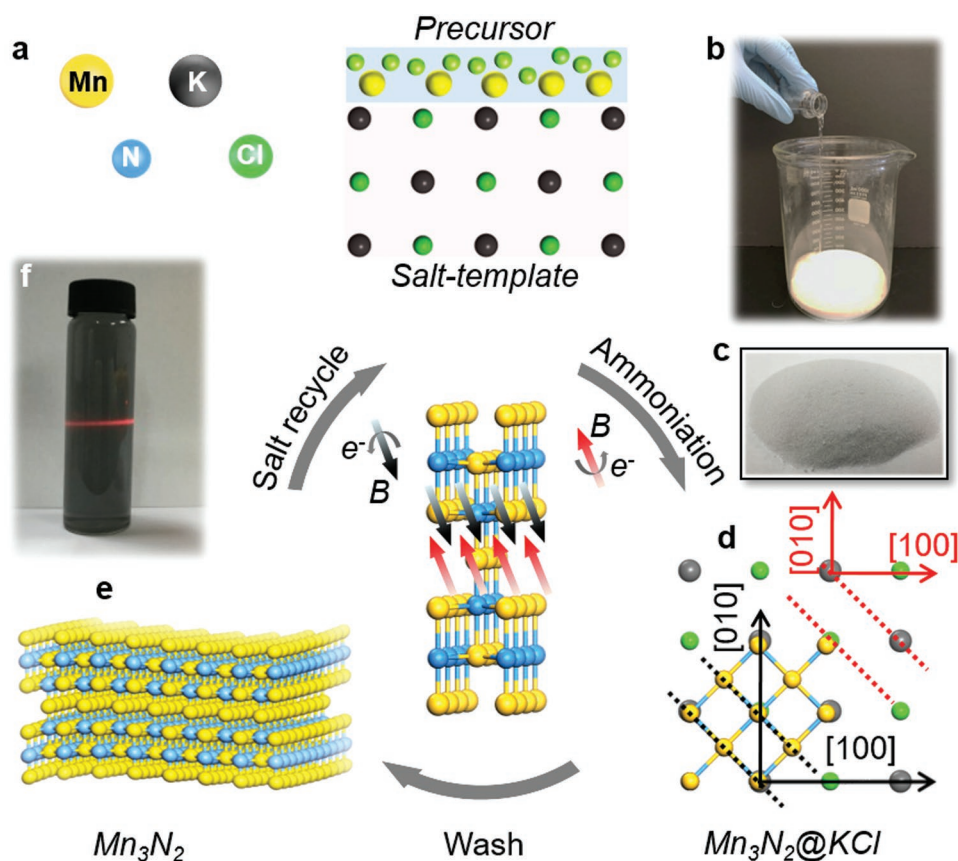


**Figure 1.** a) Schematic of synthesis. The  $\text{MnCl}_2$  solution in ethanol was coated on the surface of the KCl salt template and dried in an oven, forming a  $\text{MnCl}_2@\text{KCl}$  powder, as shown in b). c) Then, the  $\text{MnCl}_2@\text{KCl}$  powder was transferred to a furnace and treated at high temperature under a constant flow of ammonia. The ammoniation reaction transformed  $\text{MnCl}_2@\text{KCl}$  into 2D  $\text{Mn}_3\text{N}_2@\text{KCl}$ . After ammoniation, the color of the powder turned into light grayish. d) The proposed growth mechanism. We placed  $\text{Mn}_3\text{N}_2$  atomic structure on the top surface of KCl. The lattice parameter of  $\text{Mn}_3\text{N}_2$  in the [110] direction is close to that of KCl in the [110] direction. The atomic configurations closely match, hence the heteroepitaxial growth mechanism can be proposed. e) After dissolving the salt template in deionized water, the ultrathin  $\text{Mn}_3\text{N}_2$  flakes could be dispersed in water to form a black colloidal solution, which is confirmed by the Tyndall effect f).

Information). As shown in Figure 1d, when  $\text{Mn}_3\text{N}_2$  is placed on the top surface of KCl, it is seen that the lattice parameter of the  $\text{Mn}_3\text{N}_2$  (110) facet (black-dashed lines) is very close to that of KCl (220) facet (red-dashed lines). The lattice match between the surface of the KCl crystal and  $\text{Mn}_3\text{N}_2$  could facilitate the growth of 2D  $\text{Mn}_3\text{N}_2$  on the surface of KCl.

## 2. Characterizations of 2D $\text{Mn}_3\text{N}_2$

To characterize the morphology and crystal structure of 2D  $\text{Mn}_3\text{N}_2$ , bright-field transmission electron microscopy (TEM) and scanning electron microscopy (SEM) were applied. As shown in Figure 2a and Figure S6 in the Supporting Information, the as-synthesized ultrathin  $\text{Mn}_3\text{N}_2$  flakes have a rectangular shape with lateral size larger than 1  $\mu\text{m}$  and thickness in the range of 1.37 to 4.24 nm (around 1 to 3 unit cells) as measured by atomic force microscopy (AFM) and TEM (Figure S7, Supporting Information). Furthermore, the selected area electron diffraction (SAED, Figure 2b) exhibited a single-crystal pattern with a square symmetry on the [001] zone axis (*c*-axis of the unit cell), which corresponds to the (110) *d*-spacing of  $\text{Mn}_3\text{N}_2$  (2.1 Å). The high-resolution TEM image in Figure 2c presents the (110) lattice planes with a square symmetry on the same [001] zone axis. In an effort to reveal the atomic configuration and chemical composition of the  $\text{Mn}_3\text{N}_2$  flakes, we

employed an aberration-corrected high-angle annular dark-field (HAADF) scanning transmission electron microscope (STEM) equipped with an electron energy loss spectrometer (EELS). Figure 2d presents an atomic-scale HAADF-STEM image of a  $\text{Mn}_3\text{N}_2$  flake in another region on the [010] zone axis (*b*-axis of the unit cell). The corresponding Fourier transform in Figure 2e shows the *d*-spacings of 2.5 and 3.1 Å with an angle of about 53°, which matches reasonably well with the theoretical *d*-spacing values of 2.40 and 3.03 Å of (103) and (004), respectively, with an angle of 53.6°, on the same [010] zone axis, based on the standard X-ray diffraction (XRD) pattern of  $\text{Mn}_3\text{N}_2$  (PDF #01-087-2438). Since HAADF-STEM images reflect the Z-contrast of materials (Intensity  $\propto Z^{1.7}$ ),<sup>[21]</sup> it can be inferred that the bright spots are Mn atoms with hexagonal-like symmetry (marked by the white-dashed box), which is consistent with the projected crystal model in Figure 2f. It should be noted that the small difference between the STEM image and the projected crystal model (Figure 2d,f) is likely due to the sample in STEM image being slightly tilted off from the zone axis. However, it can still be inferred that the atomic arrangement shown is that of  $\text{Mn}_3\text{N}_2$ . We further acquired the atomic-scale EELS elemental maps of Mn on the [010] zone axis (Figure S8, Supporting Information). Atomic-scale Mn maps were confirmed using Mn  $L_3$  edge, which demonstrated the location of Mn atoms in the crystal structure (Figure 2h). In addition, the existence of N was confirmed by high-resolution X-ray

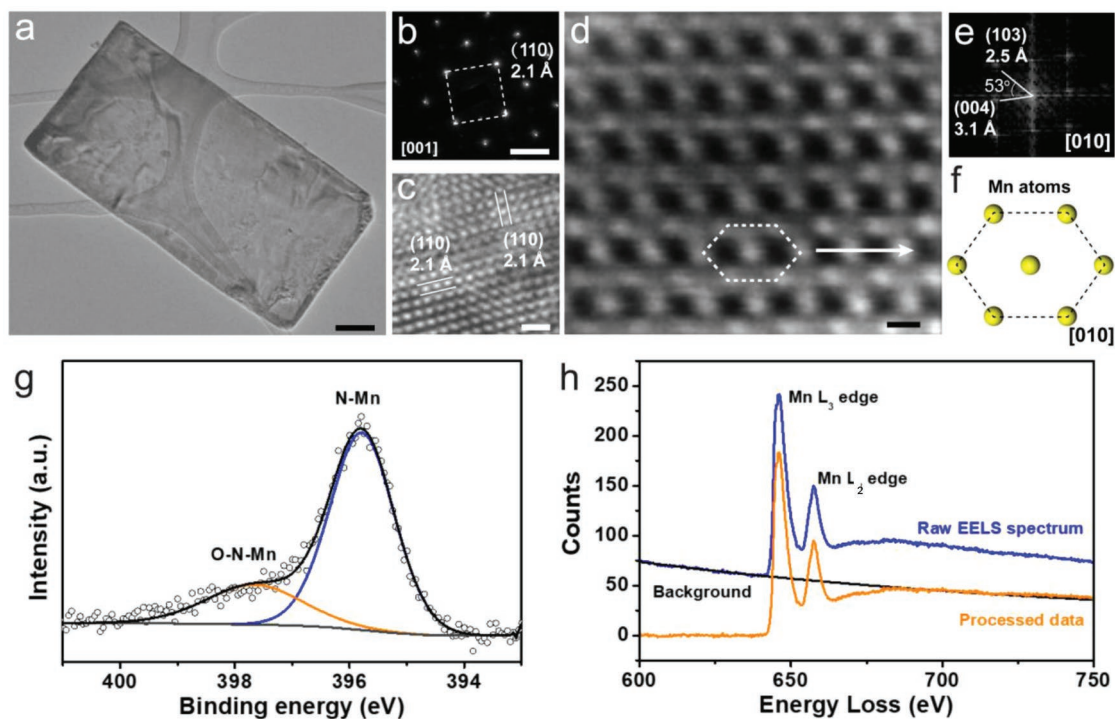


**Figure 2.** a) Bright-field TEM image of an ultrathin  $\text{Mn}_3\text{N}_2$  single-crystal flake with the lateral dimension over 1  $\mu\text{m}$ . Scale bar: 200 nm. b) The corresponding TEM electron diffraction pattern on the [001] zone axis (*c*-axis) with the (110) *d*-spacing marked in dashed squares. Scale bar: 5  $\text{nm}^{-1}$ . c) High-resolution (HR)-TEM image of  $\text{Mn}_3\text{N}_2$  with (110) *d*-spacing in a square symmetry on the [001] zone axis. Scale bar: 0.5 nm. d) Atomic-scale HAADF-STEM image of a  $\text{Mn}_3\text{N}_2$  flake in another region on the [010] zone axis (*b*-axis). Scale bar: 0.2 nm. e) Corresponding Fourier transform with (103) and (004) *d*-spacings with an angle of 53°. f) Proposed crystal model on the [010] zone axis, showing the atomic arrangement of Mn and the hexagonal-like symmetry, matching the STEM image in (d). g) XPS spectra of N 1s, confirming the N–Mn bonding in ultrathin  $\text{Mn}_3\text{N}_2$ . h) Mn EELS spectrum showing the background subtraction (black) by a linear combination of power law method (LCPL). The sharp Mn  $L_3$  edge was integrated to form the Mn EELS map (Figure S8b, Supporting Information) after being processed by principal component analysis (PCA, 2 components).

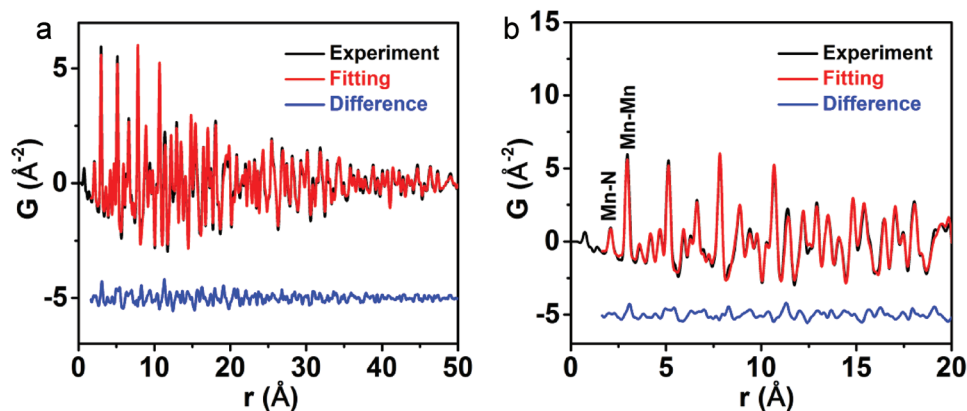


**Figure 3.** X-ray PDF analysis of  $\text{Mn}_3\text{N}_2$ . Plot b) is generated by enlarging plot a) from 0 to 20 Å. The minimal residual difference of fitting results from the proposed crystal structure (PDF# 01-087-2438) demonstrates the accuracy of the proposed  $\text{Mn}_3\text{N}_2$  structure.

photoelectron spectroscopy (XPS). The N 1s region exhibits only two peaks, which are assigned to N–Mn bonding at 395.8 eV and O–N–Mn at 397.6 eV (Figure 2g).

To obtain a more quantitative atomic structure of the material, X-ray pair distribution function (PDF) analysis was performed. The PDF,  $G(r)$ , gives the scaled probability of finding two atoms in a material at a distance  $r$  apart and is related to the density of atom pairs in the material.<sup>[22]</sup> The details of data acquisition and structural modeling<sup>[23–26]</sup> are described in the Supporting Information. Peaks in the PDF show interatomic distances in the material, for instance, the nearest Mn–N and Mn–Mn bonds are 2.10 and 2.97 Å, respectively, corresponding to PDF peaks at these positions. As shown in **Figure 3**, the PDF of the  $\text{Mn}_3\text{N}_2$  model agrees with the experimental data well with a low  $R_w$  (goodness of fit) value of 0.166 for fits over a range  $1.5 < r < 50$  Å. It should be noted that the refined lattice parameter  $c$  from PDF analysis is 12.4 Å (Table S1, Supporting Information), which is consistent with the  $d$ -spacing of (004) (3.1 Å) in the previous STEM image (Figure 2d,e). Although the fit to the bare  $\text{Mn}_3\text{N}_2$  model was satisfactory, there were a few of miniscule differences between the measured and the model PDFs (blue curve offset in Figure 3), which should be due to the presence of a small amount of Mn–O bonding on the surface.

To test any Mn oxides existing in the sample, we compare the similarity between the experimental PDF residual data after fitting to  $\text{Mn}_3\text{N}_2$  model and simulated PDFs of all Mn oxide entries available in the Inorganic Crystal Structure Database (ICSD),<sup>[27]</sup> which can be quantified using the Pearson product-moment correlation coefficient,  $P$ , defined by<sup>[28,29]</sup>

$$P = \frac{1}{n-1} \sum_{i=1}^n \left( \frac{x_i - \bar{x}}{\sigma_x} \right) \left( \frac{y_i - \bar{y}}{\sigma_y} \right) \quad (1)$$

where  $\bar{x}$  and  $\bar{y}$  are the mean values and  $\sigma_x$  and  $\sigma_y$  are the standard deviations of the datasets  $x$  and  $y$ , respectively. The calculated Pearson correlation coefficient  $P$  is between  $-1$  and  $1$ . The value  $1$  implies complete correlation,  $0$  implies no correlation, and  $-1$  suggests an anticorrelation. Accordingly, the higher positive  $P$  values mean higher degree of similarity. It ignores absolute scaling, but considers relative scaling and slight shifts in peak positions. Generally, the plausible candidate structures

can be identified through comparisons, which yield the  $P$  value typically in the range of 0.8 or higher.<sup>[29–31]</sup>

We first use the experimental PDF residual data after subtracting  $\text{Mn}_3\text{N}_2$  signal (the blue difference curve shown in Figure 3). The calculated Pearson correlation coefficients (Pearson Coeff. 1) of all Mn oxide structures over the range of  $1.5 \text{ Å} < r < 20 \text{ Å}$  are shown in **Table 1**. It clearly shows that only cubic MnO (space group:  $Fm\bar{3}m$ ) structure exists in the sample, and the corresponding PDF fit of  $\text{Mn}_3\text{N}_2$  + minority MnO model is shown in Figure S9 in the Supporting Information, which improves the  $R_w$  using  $\text{Mn}_3\text{N}_2$  single phase model (Figure 3). This is also consistent with XRD analysis (Figure S10, Supporting Information).

Then, to carefully examine the possibilities of any remaining Mn oxides, we used the experimental PDF residual data after subtracting  $\text{Mn}_3\text{N}_2$  and cubic MnO (space group:  $Fm\bar{3}m$ ) signals (the blue difference curve shown in Figure S9 in the Supporting Information). The resulted Pearson correlation coefficients (Pearson Coeff. 2) over the range of  $1.5 \text{ Å} < r < 20 \text{ Å}$  are shown in **Table 1**. No large Pearson coefficient is obtained, and it implies that no other Mn oxides except cubic MnO are present in the sample within the detection limit of X-ray PDF.

The presence of O-termination or oxide subphase is a common phenomenon for 2D metal nitrides and carbides because of the exposed metal atoms on the surface.<sup>[32]</sup> However, we found that the samples are very stable and samples remeasured after seven months of being stored in air resulted in identical PDFs indicating no further oxidation.

### 3. Magnetic Properties of 2D $\text{Mn}_3\text{N}_2$

The magnetic properties of 2D  $\text{Mn}_3\text{N}_2$  multilayer flakes were measured by a vibrating sample magnetometer (VSM) on a Quantum Design EverCool II Physical Property Measurement System (PPMS). A small hysteresis loop was observed at 300 K with a coercive field ( $H_c$ ) and remnant magnetization ( $M_R$ ) of 52 Oe and 0.012 emu  $\text{g}^{-1}$  ( $1.3 \times 10^{-4} \mu_B \text{ Mn}^{-1}$ ), respectively (inset in **Figure 4a**). This result was reproducible on different batches of samples with slight variation in the absolute values from batch to batch (Figure S11, Supporting Information). Saturation

**Table 1.** Summary of Pearson correlation coefficients. Pearson correlation coefficient 1 (Pearson Coeff. 1) is for all Mn oxide structures available in the ICSD tested against the experimental PDF residual data after subtracting  $\text{Mn}_3\text{N}_2$  signal. The most highly correlated model result is shown in bold. Pearson correlation coefficient 2 (Pearson Coeff. 2) is for all Mn oxide structures available in the ICSD tested against the experimental PDF residual data after subtracting  $\text{Mn}_3\text{N}_2$  and cubic MnO (space group:  $Fm\text{-}3m$ ) signals.

	ICSD#	Composition	Space group	Pearson coeff. 1	Pearson coeff. 2
1	<b>9864</b>	<b>MnO</b>	<b><math>Fm\text{-}3m</math></b>	<b>0.845102</b>	–
2	262928	MnO	$P6_3mc$	0.024373	0.080217
3	643187	$\text{MnO}_2$	$P4_2/mnm$	0.142454	0.262867
4	54114	$\text{MnO}_2$	$Pbnm$	0.329405	0.152411
5	78331	$\text{MnO}_2$	$Pnam$	0.350382	0.322325
6	171866	$\text{MnO}_2$	$Pnma$	0.312683	0.351751
7	248071	$\text{MnO}_2$	$Fddd$	0.118750	0.150613
8	20227	$\text{MnO}_2$	$I4/m$	0.056681	0.299154
9	76430	$\text{MnO}_2$	$P6_3/mmc$	0.142663	0.131754
10	193445	$\text{MnO}_2$	$Fd\text{-}3m$	0.084007	0.309314
11	9090	$\text{Mn}_2\text{O}_3$	$Pcab$	0.273383	0.103257
12	187263	$\text{Mn}_2\text{O}_3$	$la\text{-}3$	0.275256	0.123508
13	24342	$\text{Mn}_2\text{O}_3$	$Pbca$	0.273653	0.103915
14	236254	$\text{Mn}_2\text{O}_3$	$R\text{-}3$	0.381337	0.333974
15	236255	$\text{Mn}_2\text{O}_3$	$F\text{-}1$	0.378374	0.222398
16	33647	$\text{Mn}_2\text{O}_3$	$I2_13$	0.235979	0.071009
17	412046	$\text{Mn}_2\text{O}_3$	$Fd\text{-}3m$	0.090581	0.324806
18	60821	$\text{Mn}_2\text{O}_7$	$P2_1/c$	0.236555	0.176452
19	30005	$\text{Mn}_3\text{O}_4$	$Pbcm$	0.150406	0.160345
20	40110	$\text{Mn}_3\text{O}_4$	$Pmab$	0.408777	0.306682
21	68174	$\text{Mn}_3\text{O}_4$	$I4_1/amd$	0.397965	0.423120
22	16956	$\text{Mn}_5\text{O}_8$	$C2/m$	0.285638	0.100766

of the magnetization was not attained at an applied magnetic field of 80 kOe (8 Tesla) at 300 K as shown in Figure S12a in the Supporting Information. The combined presence of a hysteresis loop and the modest magnetization values suggest predominantly antiferromagnetic behavior of our 2D  $\text{Mn}_3\text{N}_2$ , which may be similar to its bulk counterpart and thin films where the magnetic moment is ferromagnetically aligned within (001) planes, but antiferromagnetic between neighboring (001) planes.<sup>[13,33–36]</sup> In this situation, uncompensated surface spins could be largely responsible for the measured magnetization. The  $H_c$  and  $M_R$  values measured in our 2D  $\text{Mn}_3\text{N}_2$  at 300 K are comparable to  $\text{Mn}_3\text{N}_2$  thin films on  $\text{Si}_3\text{N}_4$  and  $\text{LaAlO}_3$  and larger than edge-state induced magnetism in transition metal chalcogenides.<sup>[37–39]</sup> To exclude the possibility that the magnetic signal may come from impurities, we performed several control experiments to confirm that the coercivity and remanence observed here arise from our  $\text{Mn}_3\text{N}_2$  sample and not from any impurities. First, since there is a possible MnO impurity in the sample, we checked the magnetic properties of pure MnO (Sigma, USA; Figure S13a, Supporting Information) at room temperature and observed a linear dependence with no hysteresis loop in the range of  $-15$  to  $15$  kOe (Figure S13c, Supporting Information). Then, to exclude the possible magnetic

contaminations such as Fe, we directly oxidized the precursor ( $\text{MnCl}_2\text{@KCl}$ ) as shown in Figure S13b in the Supporting Information. If there were any Fe contamination, there should still be a hysteresis loop at room temperature after oxidation. The absence of a loop excludes the possibility of any magnetic contamination coming from iron or other uncontrolled impurities (Figure S13d, Supporting Information).

To understand if magnetism of  $\text{Mn}_3\text{N}_2$  is dependent on coupling between the sheets or is intrinsic to individual flakes, we next measured zero-field-cooled (ZFC) and field-cooled (FC) magnetization over a temperature range from 10 to 300 K for both, powder of ultrathin  $\text{Mn}_3\text{N}_2$  nanosheets and a “monolayer film.” To produce the “monolayer film” (thickness less than 5 nm), we drop-casted a dilute 2D- $\text{Mn}_3\text{N}_2$  colloidal solution onto a porous alumina substrate as shown in Figure S6 in the Supporting Information. We note that the mass of the “monolayer film” is not known, so absolute magnetization cannot be compared between these two samples, but only the shapes of the curves. Both samples showed very similar features in the ZFC and FC curves measured at an applied magnetic field of 1000 Oe (Figure 4b,c), indicating that the magnetic properties of multilayer samples are determined by that of single flakes. The peak in the ZFC curve and the abrupt increase in the FC data below 50 K is not observed in bulk  $\text{Mn}_3\text{N}_2$ , and could possibly be attributed to exchange interactions along the surface O-bonded Mn atoms or other  $\text{MnO}_x$  impurities.<sup>[40,41]</sup> Although we did not find any other Mn oxides except MnO in our sample based on X-ray PDF analysis (pure MnO did not show this low-temperature peak in ZFC curve<sup>[42]</sup>), further polarized neutron diffraction analysis may help elucidate the nature of this low-temperature peak. The possibility of a superparamagnetic transition was excluded by measuring the monolayer film at a much lower magnetic field of 50 Oe (Figure S12b, Supporting Information). No change in ZFC/FC data was detected, indicating that this magnetization change is not related to blocking phenomena, which would be field dependent.<sup>[43]</sup>

To shed light on the magnetic properties, first-principles calculations were conducted on bare  $\text{Mn}_3\text{N}_2$  and oxygen-terminated  $\text{Mn}_3\text{N}_2$  ( $\text{Mn}_3\text{N}_2\text{O}_x$ ) slabs as shown in Figure 4d–f and Figures S14 and S15 in the Supporting Information. The calculated total energies of different magnetic ordered states are shown in Figure S14b in the Supporting Information. For both  $\text{Mn}_3\text{N}_2$  and  $\text{Mn}_3\text{N}_2\text{O}_x$  slabs, the first states (first row) have the lowest energy, indicating the most stable states. The Mn spins within each (001) layer are ferromagnetically coupled, and antiferromagnetically coupled across adjacent layers, which is similar to bulk  $\text{Mn}_3\text{N}_2$ . In addition, the obtained surface energies for  $\text{Mn}_3\text{N}_2$  and  $\text{Mn}_3\text{N}_2\text{O}_x$  are 1.91 and  $-5.49$  J  $\text{m}^{-2}$ , respectively. The terminated O atoms can decrease the surface energy, resulting in a more stable structure of  $\text{Mn}_3\text{N}_2\text{O}_x$ , as mentioned above.

The profiles of total density of states (TDOS) and partial density of states (PDOS) of  $\text{Mn}_3\text{N}_2$  and  $\text{Mn}_3\text{N}_2\text{O}_x$  are shown in Figure 4d,e. The zero bandgap in the TDOS indicates the metallic nature of both  $\text{Mn}_3\text{N}_2$  and  $\text{Mn}_3\text{N}_2\text{O}_x$ . The spin-up and spin-down parts are almost symmetrical in TDOS (black line) for both  $\text{Mn}_3\text{N}_2$  and  $\text{Mn}_3\text{N}_2\text{O}_x$ , while they are quite asymmetrical for states derived from antiferromagnetically coupled Mn sites across adjacent layers (for example, Mn1 and Mn2).

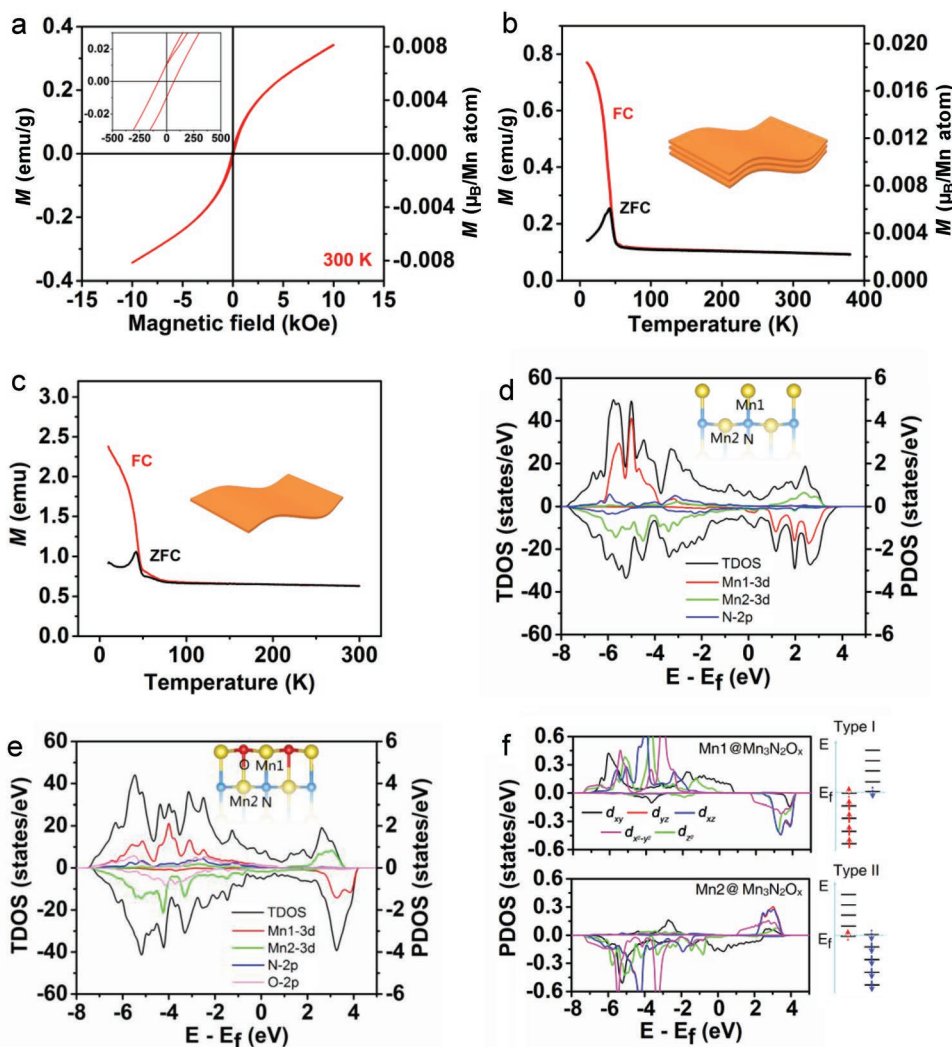


**Figure 4.** a) Magnetization hysteresis loop of multilayer ultrathin  $\text{Mn}_3\text{N}_2$  measured at 300 K. The inset shows a coercivity of 52 Oe, indicating the room-temperature magnetic behavior of ultrathin  $\text{Mn}_3\text{N}_2$ . b) Temperature dependence of zero-field-cooled (ZFC) and field-cooled (FC) magnetization of multilayer ultrathin  $\text{Mn}_3\text{N}_2$  at an applied field of 1000 Oe. c) ZFC and FC magnetization of monolayer ultrathin  $\text{Mn}_3\text{N}_2$  at an applied field of 1000 Oe. Here, we drop-cast the ultrathin  $\text{Mn}_3\text{N}_2$  colloidal solution on an AAO substrate to form the “monolayer film” shown in Figure S6 in the Supporting Information. The magnitude of the magnetization ( $y$ -axis) is multiplied by  $10^5$  for clarity. Total density of states (TDOS) and partial density of states (PDOS) for d)  $\text{Mn}_3\text{N}_2$  and e)  $\text{Mn}_3\text{N}_2\text{O}_x$ . Small yellow spheres, red and cyan are Mn, O, and N atoms, respectively. f) The splitting of Mn-3d orbitals for Mn1 and Mn2 in  $\text{Mn}_3\text{N}_2\text{O}_x$ , and two types of splitting.

The Mn 3d states are spin split, indicating that the magnetic properties of 2D  $\text{Mn}_3\text{N}_2$  and  $\text{Mn}_3\text{N}_2\text{O}_x$  originate from Mn atoms, similar to bulk  $\text{Mn}_3\text{N}_2$  (Figure S15, Supporting Information). Here, we mainly focus on the more stable and probably more realistic  $\text{Mn}_3\text{N}_2\text{O}_x$  to understand the details of the magnetism. The PDOS of five Mn-3d orbitals ( $d_{xy}$ ,  $d_{xz}$ ,  $d_{yz}$ ,  $d_{x^2-y^2}$ , and  $d_{z^2}$ ) for Mn1 and Mn2 in  $\text{Mn}_3\text{N}_2\text{O}_x$  (Mn1@ $\text{Mn}_3\text{N}_2\text{O}_x$  and Mn2@ $\text{Mn}_3\text{N}_2\text{O}_x$ ) are shown in Figure 4f. The splitting of spin is obvious. For example, the spin-up orbitals of  $d_{xz}$ ,  $d_{yz}$ ,  $d_{x^2-y^2}$ , and  $d_{z^2}$  for Mn1@ $\text{Mn}_3\text{N}_2\text{O}_x$  are fully filled, while  $d_{xy}$  is partially filled. On the other hand, the spin-down orbital of  $d_{xy}$  is partially filled, while  $d_{xz}$ ,  $d_{yz}$ ,  $d_{x^2-y^2}$ , and  $d_{z^2}$  are empty. It could be reasonably inferred that there are two types of splitting for all of the Mn atoms as shown in the right schematic of Figure 4f, resulting in the Mn moments which are in the same spin

direction within each (001) layer while in the opposite spin direction across adjacent layers.

## 4. Conclusion

In conclusion, we report high-yield synthesis of ultrathin 2D-like  $\text{Mn}_3\text{N}_2$  using a salt-templating method. The lattice of KCl salt matches well with the lattice of  $\text{Mn}_3\text{N}_2$ , allowing the growth of single crystalline 2D  $\text{Mn}_3\text{N}_2$  on the surface of KCl.  $\text{Mn}_3\text{N}_2$  flakes represent the first solution-processed ultrathin transition metal nitride with magnetism at room temperature. Theoretically, we find that the magnetic ordering results in spin-splitting of the Mn-3d derived states, and equivalent moments in opposite spin directions are symmetrically

distributed in the adjacent layers, resulting in antiferromagnetic coupling between them. This intrinsic room-temperature 2D magnet may contribute to not only the fundamental understanding of magnetism but also a practical methodology in fabricating devices with layered antiferromagnetism. Although  $\text{Mn}_3\text{N}_2$  is just the first magnetic metal nitride synthesized by this method, with further understanding of the underlying processes and identification of proper precursors and salt templates, other solution-processable 2D magnetic metal nitrides, especially with room-temperature ferromagnetism, may be produced.

## 5. Experimental Section

**Synthesis of Ultrathin  $\text{Mn}_3\text{N}_2$ :** A salt-templating method, which was developed previously,<sup>[18,20]</sup> was used for the synthesis. Typically, 17 mg  $\text{MnCl}_2 \cdot 4\text{H}_2\text{O}$  (Sigma-Aldrich, USA) was dissolved in 20 mL ethanol (95%) to form  $\text{MnCl}_2$  precursor solution in ethanol. The transparent  $\text{MnCl}_2$ /ethanol precursor solution was poured into 200 g KCl (Sigma-Aldrich, USA) and stirred vigorously. After mixing,  $\text{MnCl}_2$ @KCl was placed in an oven (70 °C) to evaporate ethanol. After that, the  $\text{MnCl}_2$ @KCl powder was treated at 750 °C for 7 h (temperature ramping rate 1 °C min<sup>-1</sup>) under a constant flow of ammonia (700 sccm) in a high-temperature furnace (Thermo Scientific). After the sample naturally cooled down to room temperature, the 2D  $\text{Mn}_3\text{N}_2$ @KCl powder was dissolved in large amount of DI water and the vacuum filtration was used to remove the KCl salt template. The solution was collected and filtrated and it was put in an oven at 70 °C, allowing the water to evaporate to recycle the KCl salt template. Finally, the ultrathin  $\text{Mn}_3\text{N}_2$  powder was dispersed in DI water. After filtration and drying, ultrathin  $\text{Mn}_3\text{N}_2$  was produced.

**Characterization:** Transmission electron microscopy was performed using a JEM-2100 (JEOL, Japan) with an accelerating voltage of 200 kV. Scanning electron microscopy was performed in a Zeiss Supra 50VP (Carl Zeiss SMT AG, Oberkochen, Germany). Scanning transmission electron microscopy images and elemental electron energy loss spectroscopy maps were acquired on a fifth-order aberration-corrected STEM (Cornell Nion UltraSTEM) operated at 100 keV with a beam convergence semiangle of 30 mrad. Sub-Ångström spatial resolution was achievable under such operating conditions. STEM images were processed using Richardson–Lucy deconvolution (three iterations) to remove the scan noise. EELS spectrum images were acquired with a 0.25 eV per channel energy dispersion in a Gatan spectrometer with a size of 100 pixels × 100 pixels and an acquisition time of 10 ms pixel<sup>-1</sup>. The Mn map was extracted using Mn  $L_3$  edge from EELS spectrum image and processed using principal component analysis (PCA, 2 components) and the linear combination of power law (LCPL) background subtraction in ImageJ software. Atomic force microscopy was performed using Bruker Multimode 8 with a Si tip (Budget Sensors Tap300A1-G;  $f_0 = 300$  kHz,  $k = 40$  N m<sup>-1</sup>) in a standard tapping mode in air. X-ray diffraction was carried out using a Rigaku Smartlab (Tokyo, Japan) diffractometer with Cu-K $\alpha$  radiation (40 kV and 44 mA) with a step scan 0.02°, a step time of 1 s, and a 10 × 10 mm<sup>2</sup> window slit. X-ray photoelectron spectroscopy spectra were measured by a spectrometer (Physical Electronics, VersaProbe 5000, Chanhassen, MN) employing a 100  $\mu\text{m}$  monochromatic Al K $\alpha$  X-ray beam to irradiate each sample's surface. Photoelectrons were collected at a takeoff angle of 45° between the sample surface of each sample and the path to the analyzer. Charge neutralization was applied using a dual beam charge neutralizer irradiating low-energy electrons and ion beam to minimize the shift in the recorded binding energy. The X-ray total scattering experiments for X-ray pair distribution function analysis were carried out at the beamline 28-ID-2 (XPD) at the National Synchrotron Light Source II (NSLS-II) at Brookhaven National Laboratory using the rapid acquisition PDF method (RAPDF).<sup>[23]</sup> A 2D Perkin Elmer amorphous silicon detector (2048 pixels × 2048 pixels and

200 × 200  $\mu\text{m}^2$  pixel size) was placed 201 mm behind the sample which was loaded in a 1 mm ID kapton capillary. The incident wavelength of the X-ray was  $\lambda = 0.1867$  Å. Calibration of the experimental setup was done using Ni as a standard material to calibrate the sample-to-detector distance and to determine the  $Q_{\text{damp}}$  and  $Q_{\text{broad}}$  parameters, which correct the PDF envelope function for the instrument resolution.<sup>[24,25]</sup> The refined values  $Q_{\text{damp}} = 0.035$  Å<sup>-1</sup> and  $Q_{\text{broad}} = 0.017$  Å<sup>-1</sup> were fixed in the subsequent structure refinements of the PDF data. A model  $\text{Mn}_3\text{N}_2$  was built based on the tetragonal  $\text{Mn}_3\text{N}_2$  phase. The space group of crystal structure is  $I4/mmm$ . The atoms are sitting at the following Wyckoff positions: Mn1 at 2a (0,0,0), Mn2 at 4e (0,0,z), N at 4e (0,0,z).

**Theoretical Calculations:** First-principles calculations were performed using VASP code,<sup>[44]</sup> based on density-functional theory (DFT).<sup>[45,46]</sup> The 2 × 2 supercells of  $\text{Mn}_3\text{N}_2$  or  $\text{Mn}_3\text{N}_2\text{O}_x$  slab with thickness around 1.3 nm were chosen to discuss their magnetic properties. The  $c$  axes parameter were set as 30 Å to ensure enough vacuum to avoid interactions between two periods. The exchange–correlation energy was calculated using general gradient approximation (GGA) with the Perdew–Burke–Ernzerhof (PBE) exchange–correlation function.<sup>[47]</sup> To have a better characterization of the localization of transition metal d electrons and a better description of their energetic, electronic, and magnetic properties, GGA + U approach with  $U - J = 3.9$ <sup>[48,49]</sup> was employed in calculations. The plane wave cutoff energy is 500 eV, and the k-point meshes of 5 × 5 × 1 and 11 × 11 × 1 in the Monkhorst Pack<sup>[50]</sup> sampling scheme were used for geometry optimization and electronic self-consistent computation, respectively. The convergence condition for the energy is 10<sup>-4</sup> eV, and the structures were relaxed until the force on each atom was less than 0.01 eV Å<sup>-1</sup>. Spin polarization was considered in all calculations. And the structure drawing and charge density visualization were generated using VESTA.<sup>[51]</sup>

Surface energies  $\gamma$  are defined as

$$\gamma = (E_{\text{slab}} - NE_{\text{unit}}/3 + N_{\text{N}}E_{\text{N}} - N_{\text{O}}E_{\text{O}})/(2A) \quad (2)$$

where,  $E_{\text{slab}}$  is the total energy of the slab,  $E_{\text{unit}}$  is the total energy per unit of  $\text{Mn}_3\text{N}_2$  in the bulk;  $N$  is the total number of Mn atoms contained in the slab model;  $N_{\text{N}}$  is the number of absent N atoms,  $E_{\text{N}} = 1/2 E_{\text{N-N}}$ , and  $E_{\text{N-N}}$  indicates the total energy of dimer  $\text{N}_2$ ;  $N_{\text{O}}$  is the number of terminated O atoms,  $E_{\text{O}} = 1/2 E_{\text{O-O}}$ , and  $E_{\text{O-O}}$  indicates the total energy of dimer  $\text{O}_2$ ; and  $A$  is the surface area.

**Magnetic Measurements:** Magnetic properties of multilayer ultrathin  $\text{Mn}_3\text{N}_2$  were studied by a vibrating sample magnetometer of a Quantum Design EverCool II Physical Property Measurement System. Prior to the measurement, sample preparation was done using a nonmagnetic labware to ensure that there was no magnetic contamination. Finely ground ultrathin  $\text{Mn}_3\text{N}_2$  powder with 1.607 mg in mass was packed in a nonmagnetizable plastic sample holder. The sample was cooled down from room temperature to 10 K at 10 K min<sup>-1</sup> in a low pressure helium environment. To obtain ZFC and FC curves, the magnetic field of 1000 Oe was applied to the sample while the temperature was linearly swept from 10 to 380 K at 4 K min<sup>-1</sup>. The M versus H loop was recorded at 300 and 10 K by sweeping magnetic field from -80 to 80 kOe at 100 Oe s<sup>-1</sup>. For the monolayer sample, a superconducting quantum interference device (SQUID) was also used. Multiple monolayer films described in the manuscript were stacked back to back to enhance signal to noise in the sample and loaded into a nonmagnetizable plastic sample holder. The sample was cooled down from 298 to 10 K at 25K min<sup>-1</sup> in the standard PPMS environment (low pressure helium). ZFC and FC measurements for the monolayer samples were carried out identically to the multilayer samples, however only heated to 300 K at 5 K min<sup>-1</sup>.

## Supporting Information

Supporting Information is available from the Wiley Online Library or from the author.

## Acknowledgements

X.X., P.U., and K.H. contributed equally to this work. The authors would like to thank Dr. Babak Anasori, Dr. Narendra Kurra, and Mr. Tyler Mathis for SEM analysis and Ms. Asia Sarycheva for AFM measurement (all at Drexel University). This work was supported by a grant from the office of Basic Energy Sciences, U.S. Department of Energy (DE-SC0018618). P.U. was supported by the U.S. National Science Foundation under grant number DMR-1310245. Y.Y. performed HAADF-STEM imaging and EELS analysis under the guidance of H.D.A. We acknowledge the Cornell Center for Materials Research (CCMR) for the use of TEM facilities which are supported through the National Science Foundation Materials Research Science and Engineering Center (NSF MRSEC) program (DMR-1719875). Y.Y. is grateful to Malcolm (Mick) Thomas at CCMR for the help with Nion UltraSTEM. X-ray PDF measurements were conducted on beamline 28-ID-2 of the National Synchrotron Light Source II, a U.S. Department of Energy (DOE) Office of Science User Facility operated for the DOE Office of Science by Brookhaven National Laboratory under Contract No. DE-SC0012704. L.Y. and S.J.L.B.'s efforts on PDF analysis, modeling, and writing were supported by the NSF MRSEC program through Columbia in the Center for Precision Assembly of Superstratic and Superatomic Solids (DMR-1420634). The computational resources were provided by Intelligent Electronics Institute, Huazhong University of Science and Technology, China. H.W. acknowledges the financial support from the China Scholarship Council (No. 201706920081). S.H.T and S.S. acknowledge support from the NSF under Cooperative Agreement Award EEC-1160504 as part of the center for Translational Applications of Nanoscale Multiferoic Systems (TANMS).

## Conflict of Interest

The authors declare no conflict of interest.

## Keywords

2D materials, magnetism, salt template, transition metal nitrides, ultrathin flakes

Received: December 18, 2018

Revised: February 13, 2019

Published online: March 6, 2019

- [1] A. K. Geim, K. S. Novoselov, *Nat. Mater.* **2007**, *6*, 183.
- [2] Y. Yu, F. Yang, X. F. Lu, Y. J. Yan, H. ChoYong, L. Ma, X. Niu, S. Kim, Y.-W. Son, D. Feng, S. Li, S.-W. Cheong, X. H. Chen, Y. Zhang, *Nat. Nanotechnol.* **2015**, *10*, 270.
- [3] M. K. Blees, A. W. Barnard, P. A. Rose, S. P. Roberts, K. L. McGill, P. Y. Huang, A. R. Ruyack, J. W. Kevek, B. Kobrin, D. A. Muller, P. L. McEuen, *Nature* **2015**, *524*, 204.
- [4] K. Kang, K.-H. Lee, Y. Han, H. Gao, S. Xie, D. A. Muller, J. Park, *Nature* **2017**, *550*, 229.
- [5] H. Yuan, X. Liu, F. Afshinmanesh, W. Li, G. Xu, J. Sun, B. Lian, A. G. Curto, G. Ye, Y. Hikita, Z. Shen, S.-C. Zhang, X. Chen, M. Brongersma, H. Y. Hwang, Y. Cui, *Nat. Nanotechnol.* **2015**, *10*, 707.
- [6] C. Gong, L. Li, Z. Li, H. Ji, A. Stern, Y. Xia, T. Cao, W. Bao, C. Wang, Y. Wang, Z. Q. Qiu, R. J. Cava, S. G. Louie, J. Xia, X. Zhang, *Nature* **2017**, *546*, 265.
- [7] W. J. Hardy, J. Yuan, H. Guo, P. Zhou, J. Lou, D. Natelson, *ACS Nano* **2016**, *10*, 5941.
- [8] G. C. Huang, E. N.-Moratalla, D. R. Klein, R. Cheng, K. L. Seyler, D. Zhong, E. Schmidgall, M. A. McGuire, D. H. Cobden, W. Yao, D. Xiao, P. J.-Herrero, X. Xu, *Nature* **2017**, *546*, 270.
- [9] X. Wang, K. Du, Y. Y. Fredrik Liu, P. Hu, J. Zhang, Q. Zhang, M. H. S. Owen, X. Lu, C. K. Gan, P. Sengupta, C. Kloc, Q. Xiong, *2D Mater.* **2016**, *3*, 031009.
- [10] B. Li, T. Xing, M. Zhong, L. Huang, N. Lei, J. Zhang, J. Li, Z. Wei, *Nat. Commun.* **2017**, *8*, 1958.
- [11] V. Kochat, A. Apte, J. A. Hachtel, H. Kumazoe, A. Krishnamoorthy, S. Susarla, J. C. Idrobo, F. Shimojo, P. Vashishta, R. Kalia, A. Nakano, C. S. Tiwary, P. M. Ajayan, *Adv. Mater.* **2017**, *29*, 1703754.
- [12] M. Bonilla, S. Kolekar, Y. Ma, H. C. Diaz, V. Kalappattil, R. Das, T. Eggers, H. R. Gutierrez, M.-H. Phan, M. Batzill, *Nat. Nanotechnol.* **2018**, *13*, 289.
- [13] K. Wang, A. R. Smith, *Nano Lett.* **2012**, *12*, 5443.
- [14] H. Kumar, N. C. Frey, L. Dong, B. Anasori, Y. Gogotsi, V. B. Shenoy, *ACS Nano* **2017**, *11*, 7648.
- [15] M. Tabuchi, M. Takahashi, F. Kanamaru, *J. Alloys Compd.* **1994**, *210*, 143.
- [16] P. Urbankowski, B. Anasori, T. Makaryan, D. Er, S. Kota, P. L. Walsh, M. Zhao, V. B. Shenoy, M. W. Barsoum, Y. Gogotsi, *Nanoscale* **2016**, *8*, 11385.
- [17] P. Urbankowski, B. Anasori, K. Hantanasirisakul, L. Yang, L. Zhang, B. Haines, S. May, S. J. L. Billinge, Y. Gogotsi, *Nanoscale* **2017**, *9*, 17722.
- [18] X. Xiao, H. Yu, H. Jin, M. Wu, Y. Fang, J. Sun, Z. Hu, T. Li, J. Wu, L. Huang, Y. Gogotsi, *ACS Nano* **2017**, *11*, 2180.
- [19] H. Yu, X. Yang, X. Xiao, M. Chen, Q. Zhang, L. Huang, J. Wu, T. Li, S. Chen, L. Song, L. Gu, B. Y. Xia, G. Feng, J. Li, J. Zhou, *Adv. Mater.* **2018**, *30*, 1805655.
- [20] X. Xiao, H. Song, S. Lin, Y. Zhou, X. Zhan, Z. Hu, Q. Zhang, J. Sun, B. Yang, T. Li, L. Jiao, J. Zhou, J. Tang, Y. Gogotsi, *Nat. Commun.* **2016**, *7*, 11296.
- [21] A. V. Crewe, J. Wall, J. Langmore, *Science* **1970**, *168*, 1338.
- [22] T. Egami, S. J. L. Billinge, *Underneath the Bragg Peaks: Structural Analysis of Complex Materials*, 2nd ed., Elsevier, Amsterdam **2012**.
- [23] P. J. Chupas, X. Qiu, J. C. Hanson, P. L. Lee, C. P. Grey, S. J. L. Billinge, *J. Appl. Crystallogr.* **2003**, *36*, 1342.
- [24] C. L. Farrow, P. Juhas, J. W. Liu, D. Bryndin, E. S. Božin, J. Bloch, T. Proffen, S. J. L. Billinge, *J. Phys.: Condens. Matter* **2007**, *19*, 335219.
- [25] T. Proffen, S. J. L. Billinge, *J. Appl. Crystallogr.* **1999**, *32*, 572.
- [26] P. Juhás, T. Davis, C. L. Farrow, S. J. L. Billinge, *J. Appl. Crystallogr.* **2013**, *46*, 560.
- [27] G. Bergerhoff, R. Hundt, R. Sievers, I. D. Brown, *J. Chem. Inf. Model.* **1983**, *23*, 66.
- [28] J. L. Myers, A. D. Well, *Research Design and Statistical Analysis*, 3rd ed., Lawrence Erlbaum Associates, Hillsdale **2010**.
- [29] T. Dykhne, R. Taylor, A. Florence, S. J. L. Billinge, *Pharm. Res.* **2011**, *28*, 1041.
- [30] M. W. Terban, R. Dabbous, A. D. Debellis, E. Pösel, S. J. L. Billinge, *Macromolecules* **2016**, *49*, 7350.
- [31] C. S. Lewis, D. Moronta, M. W. Terban, L. Wang, S. Yue, C. Zhang, Q. Li, A. Corrao, S. J. L. Billinge, S. S. Wong, *CrystEngComm* **2018**, *20*, 223.
- [32] B. Anasori, M. R. Lukatskaya, Y. Gogotsi, *Nat. Rev. Mater.* **2017**, *2*, 16098.
- [33] J. Guerrero-Sánchez, A.-O. Mandru, K. Wang, N. Takeuchi, G. H. Cocolletzi, A. R. Smith, *Appl. Surf. Sci.* **2015**, *355*, 623.
- [34] W. R. L. Lambrecht, M. Prikhodko, M. S. Miao, *Phys. Rev. B* **2003**, *68*, 17441.
- [35] H. Yang, A. Smith, *Phys. Rev. Lett.* **2002**, *89*, 226101.
- [36] H. Yang, H. Al-Britthen, A. Smith, J. Borchers, R. Cappelletti, M. Vaudin, *Appl. Phys. Lett.* **2001**, *78*, 3860.

- [37] E. Céspedes, E. Román, Y. Huttel, J. Chaboy, J. García-López, A. de Andrés, C. Prieto, *J. Appl. Phys.* **2009**, *106*, 043912.
- [38] F. Yu, Y. Liu, M. Yang, S. Wu, W. Zhou, S. Li, *Thin Solid Films* **2013**, *531*, 228.
- [39] S. Tongay, S. S. Varnoosfaderani, B. R. Appleton, J. Wu, A. F. Hebard, *Appl. Phys. Lett.* **2012**, *101*, 123105.
- [40] L. Ren, W. Zhou, Y. Wang, M. Meng, S. Wu, S. Li, *J. Appl. Phys.* **2014**, *116*, 023906.
- [41] L. T. Tseng, Y. Lu, H. M. Fan, Y. Wang, X. Luo, T. Liu, P. Munroe, S. Li, J. Yi, *Sci. Rep.* **2015**, *5*, 9094.
- [42] X. Sun, E. Feng, Y. Su, K. Nemkovski, O. Petravic, T. Brückel, *J. Phys.: Conf. Ser.* **2017**, *862*, 012027.
- [43] M. J. Benitez, O. Petravic, H. Tüysüz, F. Schüth, H. Zabel, *Phys. Rev. B* **2011**, *83*, 134424.
- [44] G. Kresse, J. Hafner, *Phys. Rev. B* **1994**, *49*, 14251.
- [45] P. Hohenberg, W. Kohn, *Phys. Rev.* **1964**, *136*, B864.
- [46] W. Kohn, L. J. Sham, *Phys. Rev.* **1965**, *140*, A1133.
- [47] J. P. Perdew, K. Burke, M. Ernzerhof, *Phys. Rev. Lett.* **1996**, *77*, 3865.
- [48] A. Jain, G. Hautier, C. J. Moore, S. P. Ong, C. C. Fischer, T. Mueller, K. A. Persson, G. A. Ceder, *Comput. Mater. Sci.* **2011**, *50*, 2295.
- [49] C. Ling, F. Mizuno, *Chem. Mater.* **2012**, *24*, 3943.
- [50] H. J. Monkhorst, J. D. Pack, *Phys. Rev. B* **1976**, *13*, 5188.
- [51] K. Momma, F. Izumi, *J. Appl. Crystallogr.* **2008**, *41*, 653.